Journal of Solid State Chemistry 186 (2012) 182–188

Contents lists available at SciVerse ScienceDirect

Journal of Solid State Chemistry

journal homepage: www.elsevier.com/locate/jssc

Sn-doped polyhedral In_2O_3 particles: Synthesis, characterization, and origins of luminous emission in wide visible range

Yunqing Zhu, Yiqing Chen *

School of Materials Science and Engineering, Hefei University of Technology, 193 Tunxi Road, Hefei, Anhui 230009, People's Republic of China

ARTICLE INFO

Article history:
Received 17 June 2011
Received in revised form
7 November 2011
Accepted 11 November 2011
Available online 4 December 2011

Keywords:
Thermal evaporation
ITO particles
Luminous emission
Cathodoluminescence spectroscopy

ABSTRACT

Sn-doped octahedronal and tetrakaidecahedronal In_2O_3 particles were successfully synthesized by simple thermal evaporation of indium grains using SnO as dopant. Structural characterization results demonstrated that the Sn-doped tetrakaidecahedronal In_2O_3 particle had additional six {001} crystal surfaces compared with the octahedronal one. The luminous properties of both samples were characterized by photoluminescence (PL) and cathodoluminescence (CL) spectroscopy. A broad visible luminous emission around 570 nm was observed. Studies revealed that the emission consisted of three peaks of 511 nm, 564 nm, and 622 nm, which were attributed to radioactive recombination centers such as single ionized oxygen vacancy, indium interstitial, and antisite oxygen, respectively. We believe that the Sn donor level plays an important role in the visible luminous emission.

1. Introduction

As an important and well-known semiconducting oxide (TCO), indium oxide (IO) has been broadly applied to displays [1,2], organic light-emitting diodes (OLEDs) [3], solar cells [4,5], functional glass [6,7], and energy efficient windows [8,9]. Researchers have synthesized pure octahedronal IO particles and IO pyramids by liquid-phase method or by physical evaporation of indium with or without Au as catalyst [10–16]. IO octahedrons precipitated on Sn-doped indium oxide substrate were also reported [17]. The Sn-doped indium oxide known as indium tin oxides (ITO) is another kind of promising n-type transparent semiconductor material in screen display techniques [18,19]. ITO powder of high purity and fine grain size is largely in demand for the preparation of ITO targets [20,21]. However, few articles were reported on the polyhedral ITO particles.

In this article, we developed a simple thermal evaporation of indium grains to prepare Sn-doped octahedronal and tetrakaidecahedronal In_2O_3 particles using SnO as dopant without the presence of Au catalyst. Apart from photoluminescence (PL) spectroscopy, cathodoluminescence (CL) spectroscopy was also employed to characterize the luminous emission features of samples. Both samples exhibit broad visible luminous emission peak around 570 nm, which has potential application in screen display techniques.

2. Experimental section

2.1. Synthesis

The synthesis of samples was carried out in a horizontal alumina tube furnace. High purity indium grains (5 N) and a mixture of SnO powder and graphite powder (both are analytic purity) were separately placed in a ceramic boat, which was located in the heating center of alumina tube. A Si substrate was put 25 cm away from the ceramic boat to collect the products. Prior to heating, the alumina tube was sealed and pumped down to a pressure of 10^{-3} Torr. Argon (Ar) gas was then introduced with a flow rate of 40 standard cubic centimeters per minute (sccm). The temperature was increased to 1000 °C at a rate of 6 °C/min and the argon gas was switched off. A flow of argon and oxygen (O_2) gas was introduced at a flow rate of 50 sccm. The O_2 partial pressure was 5% in the Ar/O_2 carrier gas with a constant total pressure of 200 Torr. After 50 min of typical growth process, the Si substrate was cooled and removed from the furnace. A yellow layer (sample A) was found on the surface of the Si substrate. The procedure for synthesis of sample B is the same as above except that the Si substrate was 2.5 cm farther from the heating center than the case of sample A.

2.2. Characterization

The samples were characterized by field emission scanning electron microscopy (FESEM, JEOL-JSM-6700F) equipped with energy dispersive spectrometer (EDS, Link ISIS, Oxford), x-ray diffraction (XRD, D/MAX2500VL/PC), and high resolution transmission electron

* Corresponding author. Fax: +86 551 290 1362.
E-mail address: chenyq63@126.com (Y. Chen).

0022-4596/$ - see front matter © 2011 Elsevier Inc. All rights reserved.
doi:10.1016/j.jssc.2011.11.019

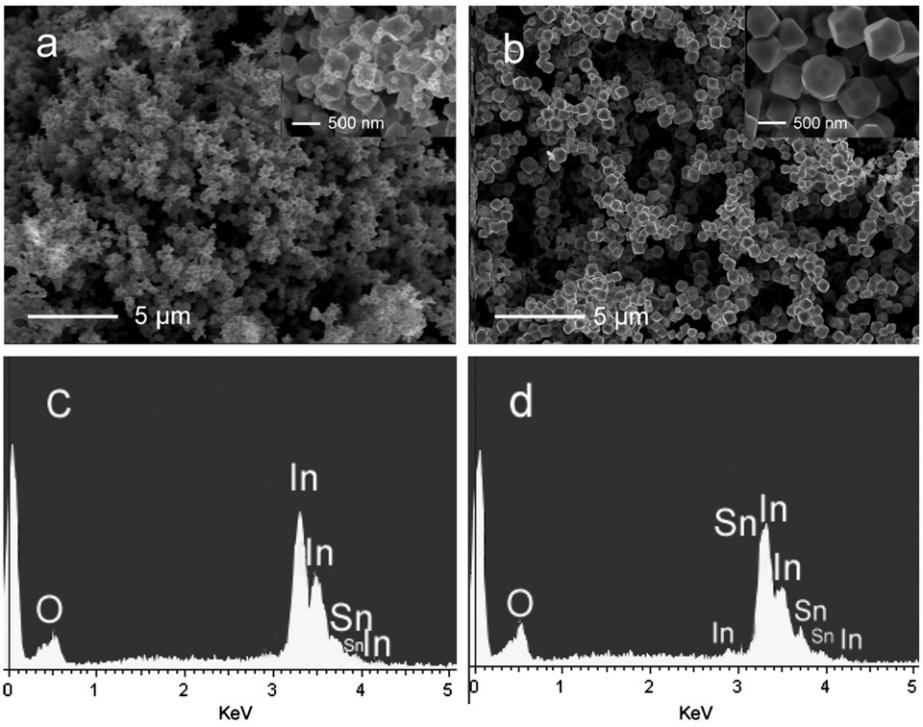

Fig. 1. FESEM images of (a) sample A and (b) sample B with high magnification images in the insets. EDS spectra (c) from sample A and (d) from sample B.

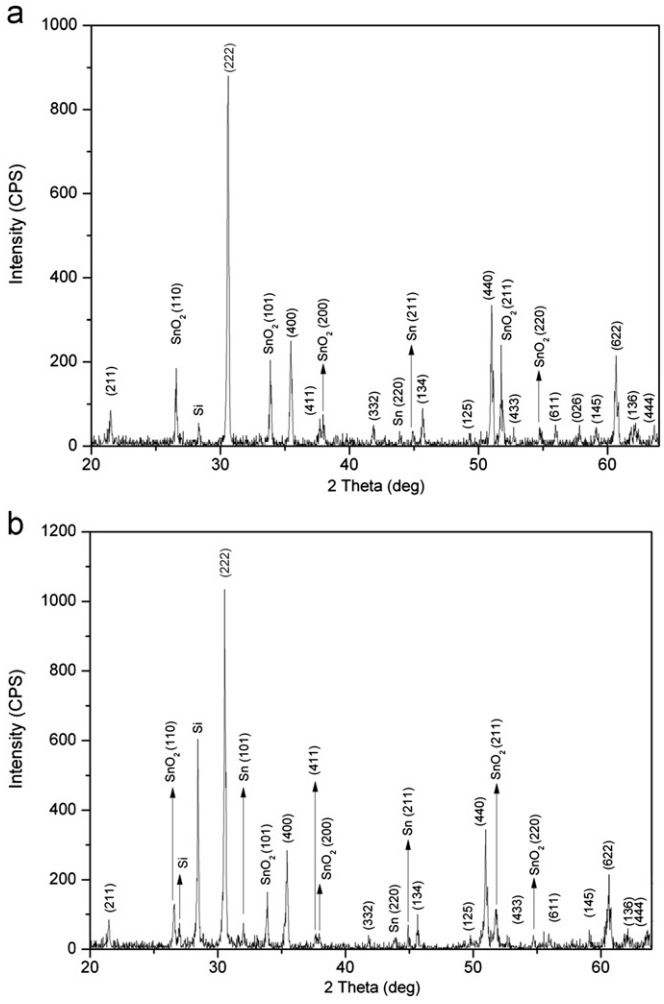

Fig. 2. XRD patterns of (a) sample A and (b) sample B.

microscopy (HRTEM, JEOL JSM-2010) equipped with EDS. PL spectroscopy was performed on a steady-state spectrofluorometer (FLUOROLOG-3-TAU) at room temperature using a He–Cd laser as the excitation source. CL spectroscopy was performed at room temperature by means of a Gatan MonoCL system attached to a scanning electron microscope. The electron paramagnetic resonance (EPR) spectra were recorded on an Electron Spin Resonance Spectrometer (JES-FA200) at a modulation frequency of 100 kHz with modulation amplitude of 0.1 mT and a sweep width of 30 mT. Raman spectra were obtained under air condition from a Laser Confocal Raman Microscope (LABRAM-RH) with an excitation wavelength of 514.5 nm.

3. Results and discussion

The morphologies of sample A and sample B are shown in Fig. 1(a) and (b), respectively. Fig. 1(a) reveals the octahedronal particles attached by tiny particles. In Fig. 1(b), the tetrakaidecahedronal particles exhibit six more surfaces than the octahedronal particles in Fig. 1(a). The diameters of two kinds of particles are averagely estimated about 450 nm. The EDS spectra of both samples were obtained under FESEM. It was found that sample A and sample B consist of elemental In, Sn, and O shown in Fig. 1(c) and (d), respectively.

XRD patterns in Fig. 2 prove that both samples are body centered cubic indium oxides phase with lattice parameter of $a=1.011$ nm (JCPDS card no. 89-4595). In the present work, SnO is utilized as dopant since the SnO can decompose to Sn and SnO_2 above 300 °C as follows: [22,23]

$$2SnO(g)=Sn(l)+SnO_2(s) \quad (1)$$

$$SnO_2(s)\rightleftharpoons SnO(g)+1/2O_2(g) \quad (2)$$

Considering the synthesis temperature of 1000 °C, it is inevitable that peaks from SnO_2 and Sn appear in the XRD patterns.

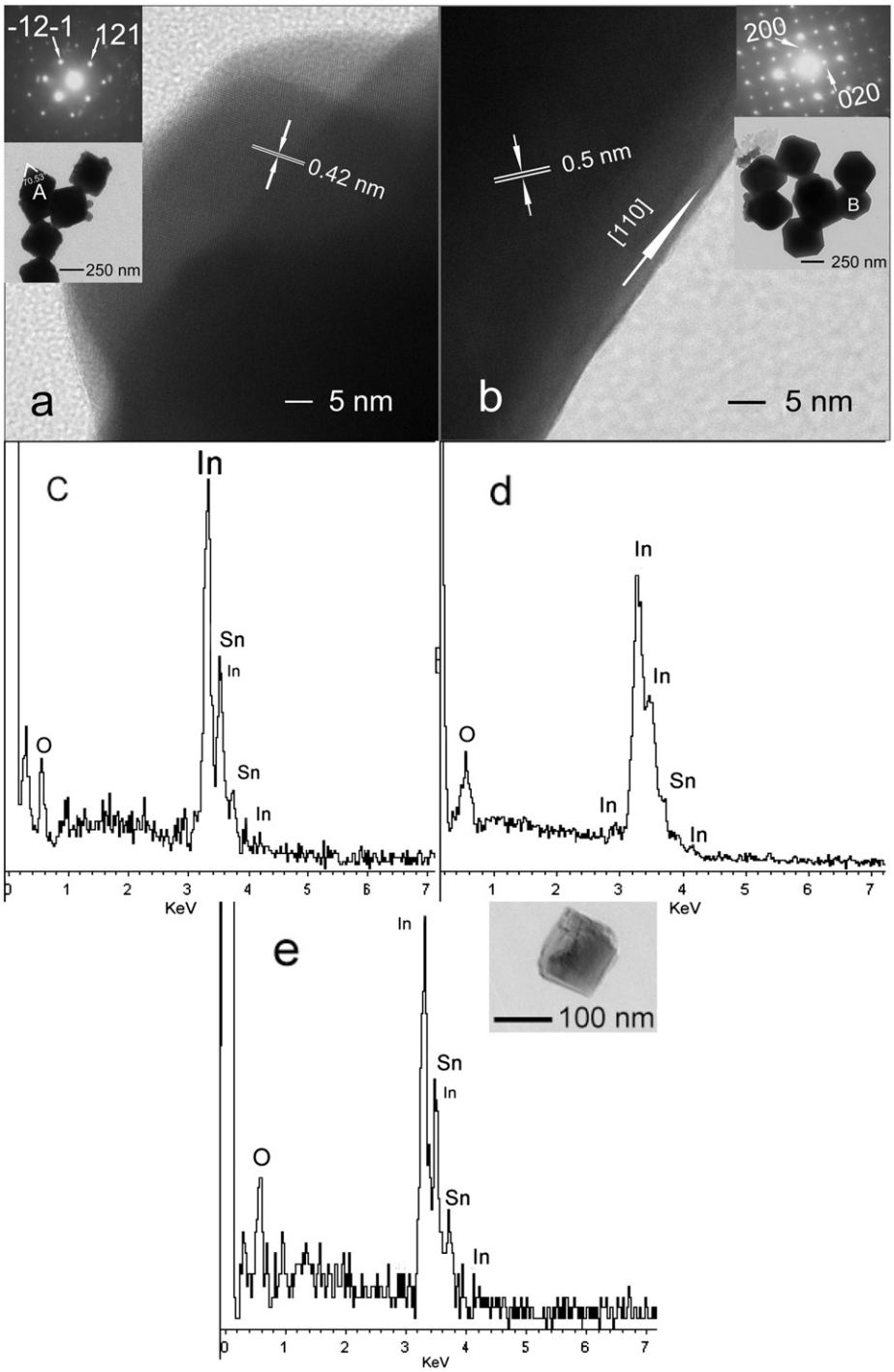

Fig. 3. HRTEM images taken from (a) octahedronal particle A and (b) tetrakaidecahedronal particle B displayed in the TEM images in the insets with corresponding SAED patterns. EDS results from (c) octahedronal particle A, (d) tetrakaidecahedronal particle B, and (e) the tiny particles in sample A (inset: TEM image of a typical tiny particle).

Fig. 3(a) and (b) is the HRTEM images of an octahedronal particle A and a tetrakaidecahedronal particle B, respectively. Corresponding selected area electron diffraction (SAED) patterns were indexed. Analysis of the HRTEM images and the SAED patterns demonstrate that both particles are single crystal. In particle A, the interplanar distance of 0.42 nm corresponds to the separation of (121) crystal face. It is in good agreement with the standard value of 0.4131 nm (JCPDS card no. 89-4595) within the measuring error. The angle between the indexed crystal face (121) and $(-12-1)$ in SAED pattern was 70.53°, which is in accord with the apex corner angle of an octahedronal structure. In particle B, the edge along [110] direction indicates that the tetrakaidecahedronal particle is grown along $<001>$ with six apex corners truncated to add six more {001} crystal surfaces than the octahedronal one. Fig. 3(c) and (d) is the point scanning EDS spectra recorded on particle A and particle B, respectively. Fig. 3(e) shows the EDS spectrum from tiny particles with a typical diameter of about 100 nm displayed in the inset. All the EDS results indicate that both kinds of particles including the tiny particles in sample A are made of In, Sn, and O. Based on the above observations, we conclude that the octahedronal particles and the tetrakaidecahedronal particles are ITO single crystal.

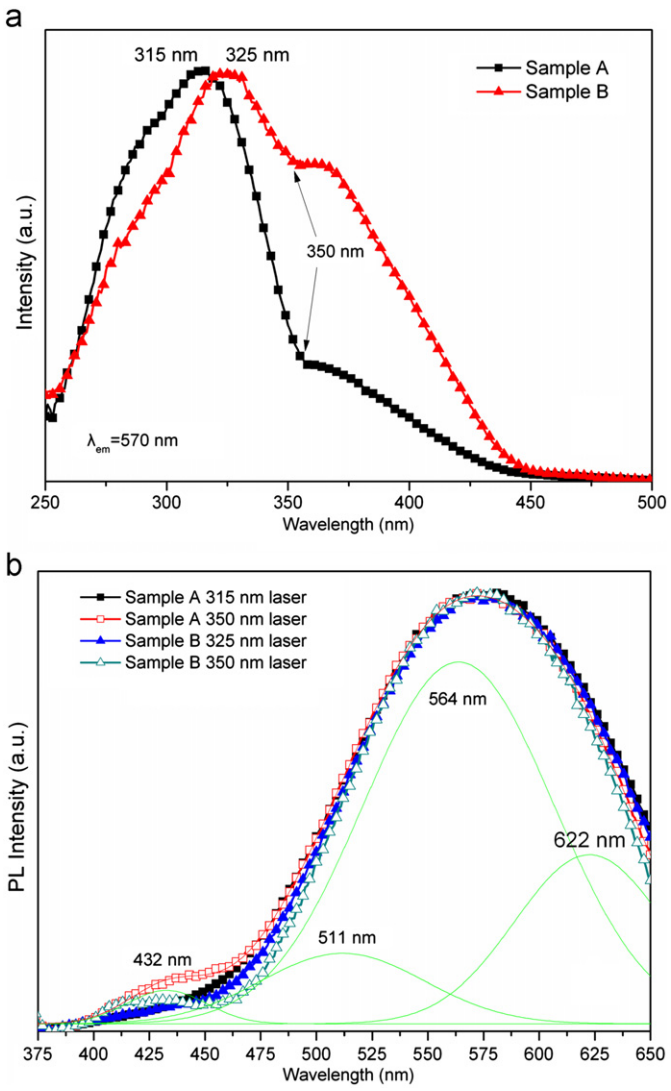

Fig. 4. (a) Excitation spectra monitored at 570 nm, (b) PL spectra excited by laser of different wavelengths. The spectrum from sample A excited by 350 nm excitation laser is selected for Gauss fit processing. All curves are normalized.

The luminous properties of samples were investigated by PL and CL spectroscopy. Fig. 4(a) is the excitation spectra monitored at 570 nm. Fig. 4(b) is the PL spectra showing a broad visible emission around 570 nm. All spectra are normalized. It can be seen in Fig. 4(a) that there are two strongest peaks at 315 nm and 325 nm for samples A and B, respectively, and two sub-strong peaks at 350 nm for both samples. The exciting wavelengths 315 nm and 325 nm are switched to 350 nm for samples A and B. Both samples exhibit two additional PL peaks at 432 nm in PL spectra shown in Fig. 4(b).

To study the local luminous emission features, CL spectroscopy was utilized. The influence of the tiny particles in sample A was specially investigated. Three test points are purposely selected from area of few tiny particles (point 2) to that of rich tiny particles (point 3) in the secondary electron images shown in Fig. 5(a) and (c). All the CL spectra also exhibit a broad visible emission band centered at around 570 nm in Fig. 5(i). No evident discrimination is detected. The results prove that the tiny ITO particles have little effect on the CL property. It was discovered that sample A had a stronger PL peak at 432 nm (2.87 eV) than that of sample B displayed in Fig. 4(b) as well as a uniform bright CL image in Fig. 5(b) and (d). In sample B, however, darkness appears in CL image as Fig. 5(f) shows. The point 5 in dark area of Fig. 5(h) has poor CL performance shown in Fig. 5(k).

The origins of luminous emission of samples were studied by analysis of various measurement results including EDS, Raman spectra, and EPR. According to the analysis of the EDS spectra recorded under HRTEM, the octahedronal and tetrakaidecahedronal particles have the atomic ratios of indium to oxygen (In:O) about 77:18 and 67:27, respectively. The nonstoichiometry is further confirmed by the Raman spectra recorded on both samples. As Fig. 6 shows, there is a strong Raman peak at 306.3 cm^{-1}, which was reported to be very sensitive to the presence of oxygen vacancies [24]. Gauss fit results exhibit two weak shoulders at 325 cm^{-1} and 329 cm^{-1} in sample A and sample B, respectively. Kumar et al. reported a shoulder peak at 321.2 cm^{-1} in octahedronal IO particles [14]. The shoulder peak can be attributed to the nonstoichiometry caused by oxygen vacancy or the quantum confinement effect [25,26]. Considering the size of the particles compared with typical Bohr radius of In_2O_3 (2.14 nm), quantum confinement effect can be ruled out in our samples. The peaks at 325 cm^{-1} and 329 cm^{-1} arise from the nonstoichiometry, which agrees with the EDS observation. Singly ionized oxygen vacancies ($V_O^{\bullet}$), which are paramagnetic F-centers, are expected to yield a single EPR signal centered near the free electron g-value (2.0023) [27]. The g factors obtained from EPR spectra in Fig. 7 indicate the existence of $V_O^{\bullet}$ in both samples. In pure IO, it has been demonstrated, by means of EPR measurements and proper thermal treatments [28,29], that a band at 430 nm (2.88 eV) originates from the oxygen vacancy, which acts as the recombination center and may introduce an acceptor level in the band gap of IO. Similar shallow acceptor level was also found by authors in the investigation into the surface of tin oxide annealed at as high as 1000 °C for 24 min. The increased band edge emission is located at 451 nm (2.75 eV) [30]. Thus, the 430 nm emission is from IO particles rather than tin oxide. However, due to Sn doping in our samples A and B, the Sn donor level is introduced into the band gap of IO particles [31]. When electrons from the donor level recombine with photon-excited holes in the valence band, the 432 nm emission can be observed in our samples [32]. Sun et al. reported a 423 nm band edge emission in ITO dots [33]. The weak blue emission at 432 nm in Fig. 4(b) is then related to Sn donor level but is not a band edge emission.

In the present work, we consider that the Sn doping plays an important role in CL performance of samples A and B. It is well-known that a pure IO crystal belongs to a cubic bixbyite-type structure (*Ia*3 space group) with two nonequivalents "*In*" sites. Three quarters of the tetrahedral sites are filled with oxygen ions. One kind of "*In*1" site is coordinated 6-fold in a regular oxygen octahedron, whereas the other "*In*2" site is surrounded by six oxygen atoms at three different distances [34]. The diameter of bivalent cations 112 pm is longer than that of the tetravalent ones 69 pm, which is close to the trivalent indium cations (80 pm) [35]. It should be easy for tetravalent tin cations from the decomposition of SnO to substitute the "*In*2" site, which results in a large repulsive force arise from the additional positive charge. The electrons will be released into the Sn donor level discussed latter to balance this extra charge [31]. These additional electrons may provide brightness in CL image of samples A and B.

The CL emission in IO samples were attributed to the oxygen vacancies or indium–oxygen vacancy centers [29,36]. In the typical CL measurement, when the cathode electron ray shoots on the samples, large amount of electrons are captured by the $V_O^{\bullet}$, which forms the donor center (V_O^{X}), which may introduce a donor level below the bottom of conductor band in IO and the electrons on acceptor levels introduced by defects will combine the holes on the top of valance band, which lead to the formation of

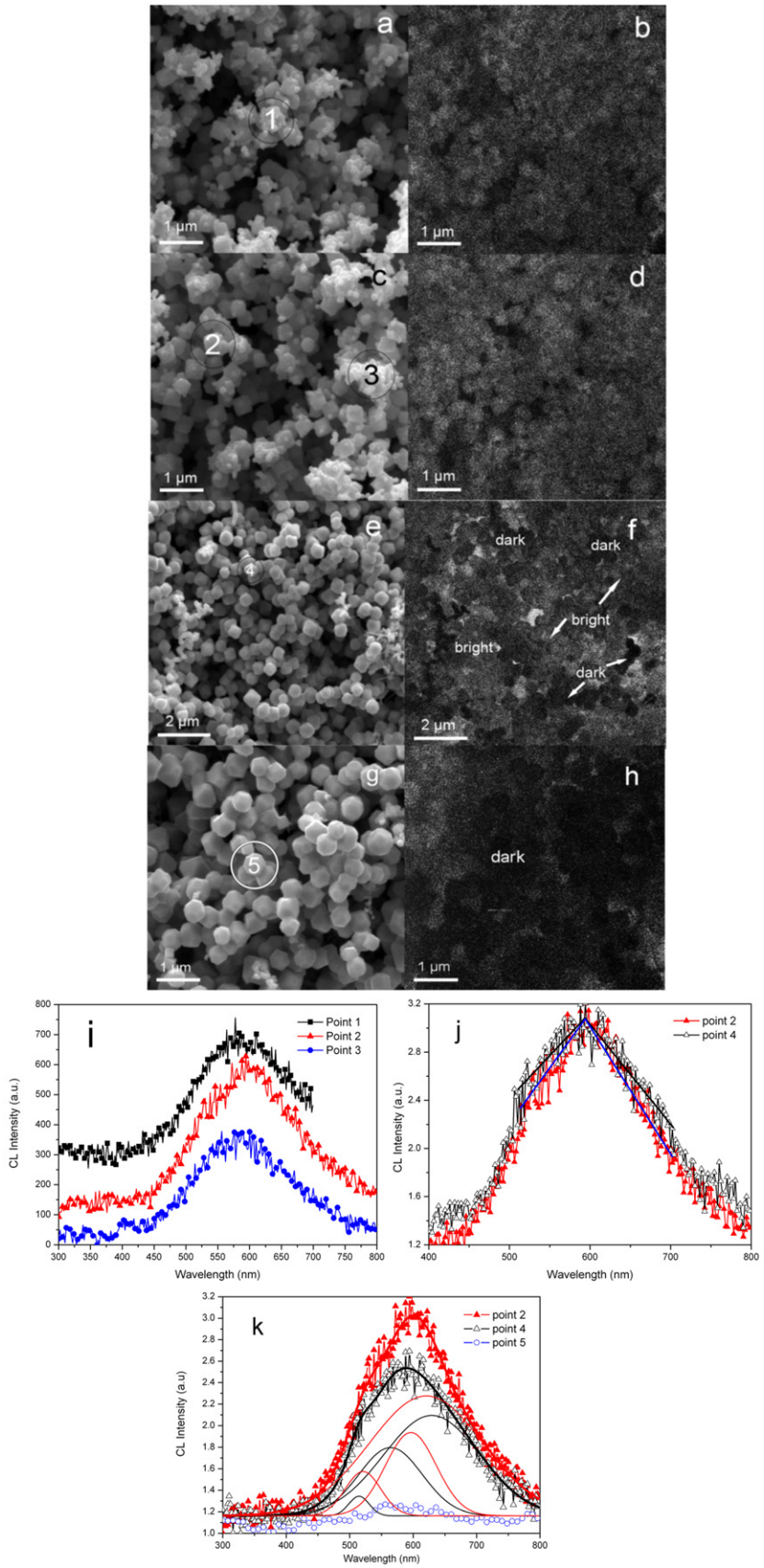

Fig. 5. Secondary electron images of (a), (c) sample A and (e), (g) sample B with corresponding CL images (b), (d) and (f), (h). (i) CL spectra of the three selected points in sample A. (j) Normalized curves point 2 and point 4 with different slops at both lower and higher energy sides. (k) Gauss fit CL spectra of point 2 in sample A and point 4 in sample B. The CL spectra from point 5 in sample B exhibits relatively low intensity.

extinction state in bandgap. When the electrons transit from the donor level to the defects levels, the emission gives out the visible CL image. In our ITO samples, the Sn donor level is considered to be significant in the role of CL performance since the additional positive charge from tetravalent tin ions. A broader EPR band in sample A was observed. It indicates a higher density of $V_O^{\bullet}$.

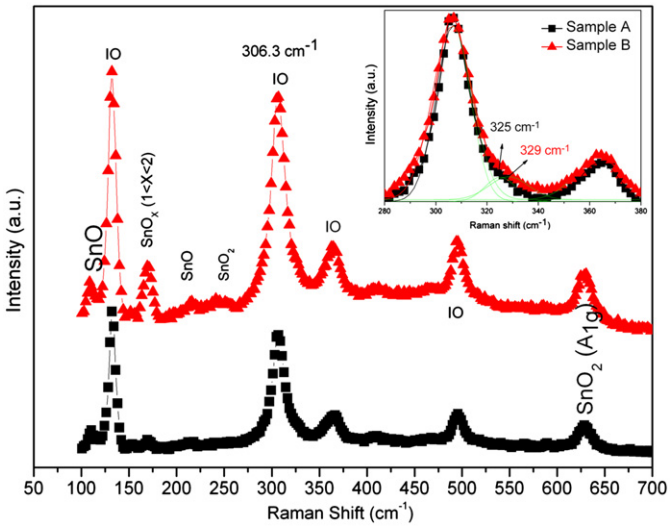

Fig. 6. Raman spectra recorded on sample A and sample B. The peaks in the 280–380 cm^{-1} range are displayed in the inset.

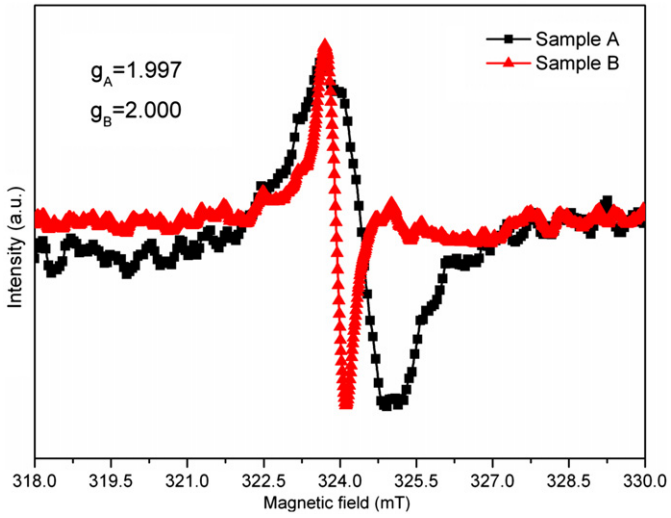

Fig. 7. EPR spectra with g factors 1.997 (sample A) and 2.000 (sample B).

According to the Heisenberg's uncertainty principle, the electron lifetime τ on a certain level and the energy difference between levels δE can be written as $\tau\delta E \sim h$. If the band width in EPR spectrum is described by the frequency width $\delta\nu$ ($\delta\nu = (\delta E/h)$), the relationship between frequency width $\delta\nu$ and lifetime τ is written as $\delta\nu \sim (1/\tau)$. Compared with sample B, the broader band width of sample A suggests a shorter lifetime of electrons on the acceptor level of $V_O^{\bullet}$. It means that the electrons can be more quickly activated to Sn donor level in sample A when exposed to the cathode ray and radiatively transit back to the acceptor level of $V_O^{\bullet}$ or other defect levels. The emission gives out an uniform bright CL image whereas the narrow EPR band width of sample B with lower density of $V_O^{\bullet}$ leads to the darkness in CL image shown in Fig. 5(f) and (h) as well as poor CL performance in Fig. 5(k).

It was reported that the visible emission band at around 590 nm IO nanowires shifts to the higher energies at ~2.9 eV since Sn doping [33]. In our ITO particles, the PL band at 432 nm(2.87 eV) appears and the PL emission at 590 nm in octahedronal IO particles shifts to higher energy side around 570 nm in our polyhedral ITO particles. There is noise in CL spectra in Fig. 5. Two curves (points 2 and 4) are normalized in Fig. 5(j). The curves exhibit different slopes in the lower energy side of the band as well as in the band in the higher energy side, which indicates that there are different contributions to the emission from both lower and higher energy sides. The Gaussian deconvolution on the band centered at around 570 nm shown in the Fig. 5(k) as well as Fig. 4(b) exhibits three Gaussian peaks at around 511 nm (2.43 eV) in the higher energy side, 564 nm (2.2 eV) near the center, and 622 nm (2 eV) in the lower energy side. Mazzera et al. pointed out that the emission band at 630 nm is referred to some possible defects such as interstitial oxygen (O_i), Indium vacancy (V_{In}) or antisite oxygen (O_{In}) rather than V_O in IO nanowires [29], and this band also shifts to higher energy side about 622 nm in our ITO particles. Therefore, we propose that the appearance of 432 nm band and blue shift of the emissions band at 590 nm and 630 nm is the consequence of Sn doping. In the experiment, oxygen gas can be from the carrier gas or the released oxygen gas shown in the chemical reaction (2). At high temperature of 1000 °C, oxygen gas will decomposed to oxygen atoms. When the oxygen atoms substitute some indium cations and form O_{In}, the indium cations become interstitials in crystal lattice. The possibility of the formation of V_{In} is then lowered. In addition, the oxygen vacancy can provide site for oxygen atom to fill in. The O_i will not greatly exist. We propose that the peak at 622 nm is assigned to O_{In} in polyhedral ITO particles. The Gaussian peak at 564 nm, which is the near the 570 nm is associated with the In_i^{3+} [14]. The intensity of Gaussian peak at 511 nm to the intensity of Gaussian peak at 622 nm is calculated based on the CL spectra in Fig. 5(k). The value was found obviously lower in sample B (0.195) than that in sample A (0.366). The low $V_O^{\bullet}$ density in sample B is probably responsible for the result.

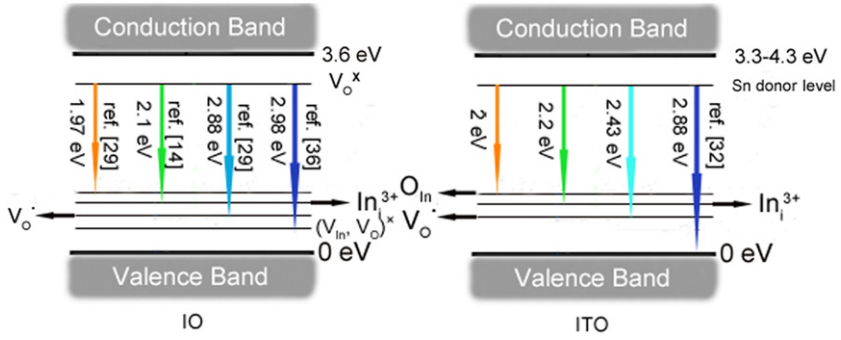

Fig. 8. Schematic diagrams of the radioactive recombination processes in IO and ITO. The reported emissions are indicated with references.

Based on the analysis above, schematic diagrams of the radioactive recombination processes in IO and ITO were derived in Fig. 8. It can be calculated that the Sn donor level in ITO is about 0.42–1.42 eV below the conduction band edge. In the tin oxide, the V_O^X donor level was demonstrated up to 0.3 eV below the bottom of conduction band by means of electron spin resonance measurements [37]. In our ITO samples, the Sn donor level is important for the luminous emission in visible range. The major part of the broad visible luminous emission originates from indium interstitial and antisite oxygen in our samples.

4. Conclusions

Sn-doped polyhedral In_2O_3 particles were synthesized by simple thermal evaporation of indium grain using SnO as dopant. The Sn-doped tetrakaidecahedronal In_2O_3 particle had six more {0 0 1} crystal faces than the octahedronal one. The Sn donor level is important for the luminous emission in visible range. The major part of the broad visible luminous emission originates from indium interstitial and antisite oxygen in our samples. With more singly ionized oxygen vacancies and tin doping, ITO particles can exhibit a better CL performance in wide visible range, which satisfies the requirement of screen display technique.

Acknowledgment

This work was financially supported by the National Natural Science Foundation of China (NSFC, No. 21071039).

References

[1] C. Falcony, J.R. Kirtley, D.J. Dimaria, T.P. Ma, T.C. Chen, J. Appl. Phys. 58 (1985) 3556.
[2] Ohta, M. Orita, M. Hirano, H. Tanji, H. Kawazoe, H. Hosono, Appl. Phys. Lett. 76 (2000) 2740.
[3] M. Kamei, T. Yagami, S. Takaki, Y. Shigesato, Appl. Phys. Lett. 64 (1994) 2712.
[4] H. Kobayashi, T. Ishida, Y. Nakato, H.J. Tsubomura, Appl. Phys. 69 (1991) 1736.
[5] M.A. Martinez, J. Herrero, M.T. Gutierrez, Thin Solid Films 269 (1995) 80.
[6] C. Xu, L. Liu, S.E. Legenski, D. Ning, M.J. Taya, Mater. Res. 19 (2004) 2072.
[7] C.G. Granqvist, A. Hulta ker, Thin Solid Films 411 (2002) 1–5.
[8] B.G. Lewis, D.C. Paine, MRS Bull. 25 (2000) 22.
[9] R.G. Gordon, MRS Bull. 25 (2000) 52.
[10] Y.B. Zhao, Z.J. Zhang, Z.S. Wu, H.X. Dang, Langmuir 20 (2004) 27.
[11] P. Guha, S. Kar, S. Chaudhuri, Appl. Phys. Lett. 85 (2004) 3851.
[12] Conference Proceedings, Society of Vacuum Coaters, USA, 1999, p. 246.
[13] M. Wei, D. Zhi, Driscoll, J. Nanotechnol. 17 (2006) 3523.
[14] M. Kumar, V. Singh, F. Singh, K.V. Lakshmi, B.R. Mehta, J.P. Singh, Appl. Phys. Lett. 92 (2008) 171907.
[15] A. Qurashia, E.M. El-Maghrabyb, T. Yamazakia, T.J. Kikutaa, J. Alloys Compd. 480 (2009) L9.
[16] T.S. Ko, C.P. Chu, J.R. Chen, Y.A. Chang, T.C. Lua, H.C. Kuo, S.C. Wang, J. Vac. Sci. Technol. A 25 (2007) 1038.
[17] M. Wei, D. Zhi, J. Driscoll, Nanotechnology 17 (2006) 3523.
[18] F.G. Li, D.P. Liu, P. Deng, Rare Met. Cemented Carbides 138 (1999) 15.
[19] R. Wang, C.C. Lee, Society of Vacuum Coaters 42nd 1999 Annual Technical.
[20] X.C. Duan, X.P. Yang, Rare Met. Cemented Carbides 138 (1999) 58.
[21] Y.F. Zhang, J.X. Zhang, J. Funct. Mater. 5 (2003) 573.
[22] M.S. Moreno, R.C. Mercader, A.G. Bibiloni, J. Phys. Condens. Matter 4 (1992) 351.
[23] M. Nagano, J. Cryst. Growth 66 (1984) 377.
[24] W.B. White, V.G. Keramidas, Spectrochim. Acta, Part A 28 (1972) 501.
[25] K. Mcguire, Z.W. Pan, Z.L. Wang, D. Milkie, J. Menéndez, A.M. Raoa, J. Nanosci. Nanotech. 2 (2002) 1.
[26] J. Zuo, C. Xu, X. Liu, C. Wang, C. Wang, Y. Hu, Y. Qian, J. Appl. Phys. 75 (1994) 1835.
[27] D.W. Cooke, M.W. Blair, J.F. Smith, B.L. Bennett, L.G. Jacobsohn, E.A. McKigney, R.E. Muenchausen, IEEE Trans. Nucl. Sci. 55 (2008) 1118.
[28] M.J. Zheng, L.D. Zhang, G.H. Li, X.Y. Zhang, X.F. Wang, Appl. Phys. Lett. 79 (2001) 839.
[29] M. Mazzera, M.Z. Zha, D. Calestani, A. Zappettini, L. Lazzarini, G. Salviati, L. Zanotti, Nanotechnology 18 (2007) 355707.
[30] J.D. Prades, J. Arbiol, A. Cirera, J.R. Morante, M. Avella, L. Zanotti, E. Comini, G. Faglia, G. Sberveglieri, Sens. Actuators B 126 (2007) 6.
[31] Y.A. Cao, W.S. Yang, W.F. Zhang, G.Z. Liu, P.L. Yue, New J. Chem. 28 (2004) 218.
[32] J. Gao, R. Chen, D.H. Li, L. Jiang, J.C. Ye, X.C. Ma, X.D. Chen, Nanotechnology 22 (2011) 195706.
[33] Z.Y. Sun, J.B. He, A. Kumbhar, J.Y. Fang, Langmuir 26 (6) (2010) 4246.
[34] M. Quaas, C. Eggs, H. Wulff, Thin Solid Films 332 (1998) 277.
[35] R.D. Shannon, Acta. Cryst. A 32 (1976) 751.
[36] X.C. Wu, J.M. Hong, Z.J. Han, Y.R. Tao, Chem. Phys. Lett. 373 (2003) 28.
[37] Y. Mizokawa, S. Nakamura, Jpn. J. Appl. Phys. 14 (1975) 779.